RSC Advances

PAPER

View Article Online
View Journal | View Issue

Cite this: *RSC Adv.*, 2015, **5**, 27649

Studies on the electrochemical intercalation/de-intercalation mechanism of $NiMn_2O_4$ for high stable pseudocapacitor electrodes†

K. Vijaya Sankar,[a] S. Surendran,[a] K. Pandi,[a] A. M. Allin,[a] V. D. Nithya,[a] Y. S. Lee[b] and R. Kalai Selvan*[a]

Received 8th January 2015
Accepted 3rd March 2015

DOI: 10.1039/c5ra00407a

www.rsc.org/advances

Sub-micron sized polyhedral shaped $NiMn_2O_4$ particles were successfully prepared by a glycine assisted solution combustion method. The phase purity and the presence of functional groups in $NiMn_2O_4$ were revealed through X-ray diffraction (XRD) and Fourier transform infrared spectroscopy (FT-IR), respectively. The formation of polyhedral shaped particles was inferred by field emission scanning electron microscopy (FE-SEM). The negative temperature coefficient of resistance (NTCR) behaviour of $NiMn_2O_4$ was observed using a solid state impedance analyser in the measured temperature range between 30 and 180 °C. Further, electrochemical studies revealed that $NiMn_2O_4$ stores the charge through intercalation rather than by a capacitive mechanism. The electrode stores 91% of the specific capacitance by intercalation and 9% by a capacitive mechanism. Also, $NiMn_2O_4$ possesses a specific capacitance of 202 F g^{-1} at 0.5 mA cm^{-2} in 1 M Na_2SO_4 electrolyte and exhibits excellent cyclic stability over 15 000 cycles. Similarly, the fabricated asymmetric device ($FeVO_4$||$NiMn_2O_4$) also delivers good specific capacitance (50 F g^{-1} at 1 mV s^{-1}) and cyclic stability.

1. Introduction

It is well known that supercapacitors or ultracapacitors have higher power density than batteries; therefore they can be used in high power applications like hybrid electrical vehicles. Based on the charge storage mechanism and the type of electrodes, they are categorised into three types such as (i) electrical double layer (EDL) capacitors, (ii) pseudocapacitors and (iii) hybrid supercapacitors. In EDL capacitors, the charge is stored by the accumulation of electronic and ionic charges at the electrode/electrolyte interface *via* electrostatic interaction. Due to the surface storage of ions, the EDL capacitor has limited energy density but it has higher power density. Various carbon based nanostructured materials are employed as electrode materials for EDL capacitors because of their large surface area and electronic conductivity. On the other hand, the pseudocapacitor stores the charge based on the fast surface redox reaction or charge transfer reaction which improves the energy density than the EDL capacitor. Consequently, the power density is less when compared with EDL capacitor. This may be due to the usage of low surface area materials and larger discharge time or battery like behaviour. In addition, the Faradaic capacitance arises generally from (i) underpotential deposition, (ii) surface redox reaction and (iii) intercalation reaction.[1] In underpotential deposition, the electroactive species from the electrolyte gets adsorbed on the surface of the electrode and undergoes redox reaction at particular potential. The surface redox reaction occurs when the electrolyte ions are adsorbed on the surface of the electrode followed by charge transfer between the electrode and electrolyte. Similarly, in intercalation/de-intercalation reaction, the electrolyte ions moved into/from the electrode matrix and undergo redox reaction.[1] In hybrid supercapacitor, both EDL capacitive and pseudocapacitive mechanisms occurs individually in positive and negative electrodes, respectively. It delivers high energy density, high specific capacitance and wider working potential window than EDL capacitor and pseudocapacitor. However, the charge and mass balancing between the electrodes is little difficult.

Various metal hydroxides, oxides (MOs) and conducting polymers (CPs) are employed as electrode material for pseudocapacitor. Use of conducting polymers for practical applications is limited due to their poor cyclic stability unlike MOs.[1–6] Therefore, the spinel structured mixed metal oxides are getting pronounced interests in recent times due to the presence of various oxidation state metal cations, multiple redox reactions,[7] improved active sites, good cyclic stability, and electronic conductivity.[8] It has been reported that various spinel ferrites, MFe_2O_4 (M = Fe, Co, Ni, Mn, Zn),[9–13] cobaltites, MCo_2O_4 (M = Co, Ni, Mn)[14–16] and manganites MMn_2O_4 (M = Mn, Co, Ni)[7,17,18] have been used as the potential electrodes for pseudocapacitors.

[a]*Solid State Ionics and Energy Devices Laboratory, Department of Physics, Bharathiar University, Coimbatore-641 046, Tamil Nadu, India. E-mail: selvankram@buc.edu.in*
[b]*Faculty of Applied Chemical Engineering, Chonnam National University, Gwangju 500-757, Korea*

† Electronic supplementary information (ESI) available. See DOI: 10.1039/c5ra00407a

In this line, the present study explored the applicability of spinel $NiMn_2O_4$ for the supercapacitor electrode. $NiMn_2O_4$ is one of the semiconducting materials and widely used as thermistor, effective catalyst for the decomposition of waste gases such as CO and N_2O and ferromagnetic material.[17,18] Literature depicts that only scarce amount of work has been reported on the application of $NiMn_2O_4$ as electrode for supercapacitors.[17,18] Especially, Pang *et al.* have prepared $NiMn_2O_4$ by calcination of oxalate precursors and investigated the effect of morphology on electrochemical properties and obtained the maximum specific capacitance of 180 F g^{-1} at 250 mA g^{-1} for porous plate like morphology.[17] Mesoporous $NiMn_2O_4$ prepared by Ren *et al.*, using two solvent methods and achieved the voltammetry specific capacitance of 94 F g^{-1} at 1 mV s^{-1}.[18] Zhang *et al.* has prepared the mesoporous $NiMn_2O_4$ using sol–gel method and obtained the specific capacitance of 243 F g^{-1} at 5 mV s^{-1} in 1 M Na_2SO_4 electrolyte.[19]

In the present work, simple glycine assisted solution combustion method was adopted to prepare $NiMn_2O_4$ particles. Since the combustion method has its own advantages over other methods like short reaction time, low ignition temperature, avoids prolonged high temperature calcination, simple experimental setup, cheap raw materials and cost effective. Eventhough, the scarce amount of work has been reported on the preparation of $NiMn_2O_4$ for pseudocapacitors, no literature describes the intercalation/de-intercalation mechanism and the amount of charge stored in inner and outer surface of the electrodes. Hence, this may be first report of its kind to explain the electrochemical charge storage mechanism using Power law and to calculate the amount of charge stored in the inner and outer surface of $NiMn_2O_4$ electrode using Trassati plot in 1 M Na_2SO_4 electrolyte. As well as it is explored the performance of the fabricated asymmetric $FeVO_4||NiMn_2O_4$ supercapacitor.

2. Experimental methods and materials

All the chemicals are of analytical grade and were used without any further purification. Stoichiometric quantities of $Ni(NO_3)_2 \cdot 4H_2O$ and $MnCl_2 \cdot 6H_2O$ were used as cation precursors and glycine was used as a fuel. The cation precursors were dissolved in minimum amount of double distilled water individually. Then, $MnCl_2 \cdot 6H_2O$ solution was added drop wise into $Ni(NO_3)_2 \cdot 4H_2O$ solution. Further, the glycine solution was added drop wise into the above mixture with continuous stirring. Subsequently, the pH of the solution was adjusted to 8 by using ammonia solution. Finally, the mixture was dehydrated at 80 °C using hot plate to obtain gel like sticky-paste. Immediately, the gel was transferred to the heater at 300 °C for the combustion reaction. During combustion, voluminous fumes come out and finally the foamy powder of $NiMn_2O_4$ was obtained. Further, the foamy powder was calcinated at 800 °C to improve the crystallinity.

The phase purity and compound formation was characterized by an X-ray Diffractometer, Bruker D8 Advance with Cu Kα radiation. The functional groups were analysed using Bruker Tensor27 FT-IR Instrument. The morphology of the material was analysed using FE-SEM (Quanta FEG 250). The electrical behaviour of the material was studied using a computer controlled impedance analyzer HIOKI 3532 LCR HITESTER in the frequency ranging from 42 Hz to 4 MHz. The powder sample was pressed into a 1 cm^{-1} diameter pellet at a pressure of 50 kg cm^{-2} under identical condition. The electrochemical analysis such as cyclic voltammogram, and galvanostatic charge–discharge were carried out using Bio-Logic SP150 electrochemical workstation.

To prepare the working electrode, $NiMn_2O_4$ active material was mixed with conductive additive (carbon black), and binder (PVDF) in the weight ratio of 80 : 15 : 5. It was mixed using NMP as a solvent (0.3 ml) and was ground well for 1 hour and coated on a 1 × 1 cm^2 stainless steel plate. The coated electrode is dried at 60 °C for overnight. The prepared electrode underwent electrochemical investigation in 1 M Na_2SO_4 electrolyte using a three electrode system. Here, Ag/AgCl and platinum wire were used as reference and counter electrodes, respectively.

3. Results and discussion

Structural and morphological properties

The single phase formation and crystal structure of $NiMn_2O_4$ was examined by XRD analysis. Fig. 1(a) shows the XRD pattern of $NiMn_2O_4$ particles. It can be seen that the observed high intensity, sharp and well defined peaks are well consistent with the standard (JCPDS no. 71-0852). Further, the observed diffraction planes are (111), (220), (311), (222), (400), (422), (511), (440), and (533) corresponding to *d*-spacing of 4.853, 2.972, 2.534, 2.421, 2.099, 1.716, 1.618, 1.485 and 1.281 Å, respectively, which confirms the single phase formation of $NiMn_2O_4$. The obtained peaks are assigned to the cubic face centred structure. The calculated lattice constant of $NiMn_2O_4$ is 8.400 Å. It is well matched with the reported value of 8.406 Å.[20–22] According to Scherrer equation,[23] the peak broadening is mainly dependent upon the grain size. For a small grain, the peak broadening is high and *vice versa*. In the present case, the XRD peaks are sharp and high intense which evidences the larger grain size of 77 nm. It is well known that large grain size particles have a lower grain boundary resistance which leads to an increase in the electrical conductivity of the material.

Further, the functional groups presence in the $NiMn_2O_4$ before and after combustion reaction was analysed using FT-IR spectra (Fig. 1(b and c)). Generally, it is used to identify the local structure of the material *via* its molecular vibrations associated with the functional groups within the material.[21,24,25] Before combustion, the $NiMn_2O_4$ precursor contains the strong band at 1382 cm^{-1} which corresponds to the characteristic vibration of NO_3^-. As well as the bands observed at 1419 cm^{-1}, 1582 cm^{-1}, and 1735 cm^{-1} infers the presence of stretching vibration of COO^-, C=C and C=O groups, respectively. On the other hand, two characteristic vibration bands observed around 600 and 400 cm^{-1} in the calcinated $NiMn_2O_4$. It is assigned to vibration mode of tetrahedral groups of Mn^{3+}–O^{2-} and octahedral group vibration of Ni^{2+}–O^2, which confirms the formation of $NiMn_2O_4$.[19,24] In addition, the vibration bands observed at

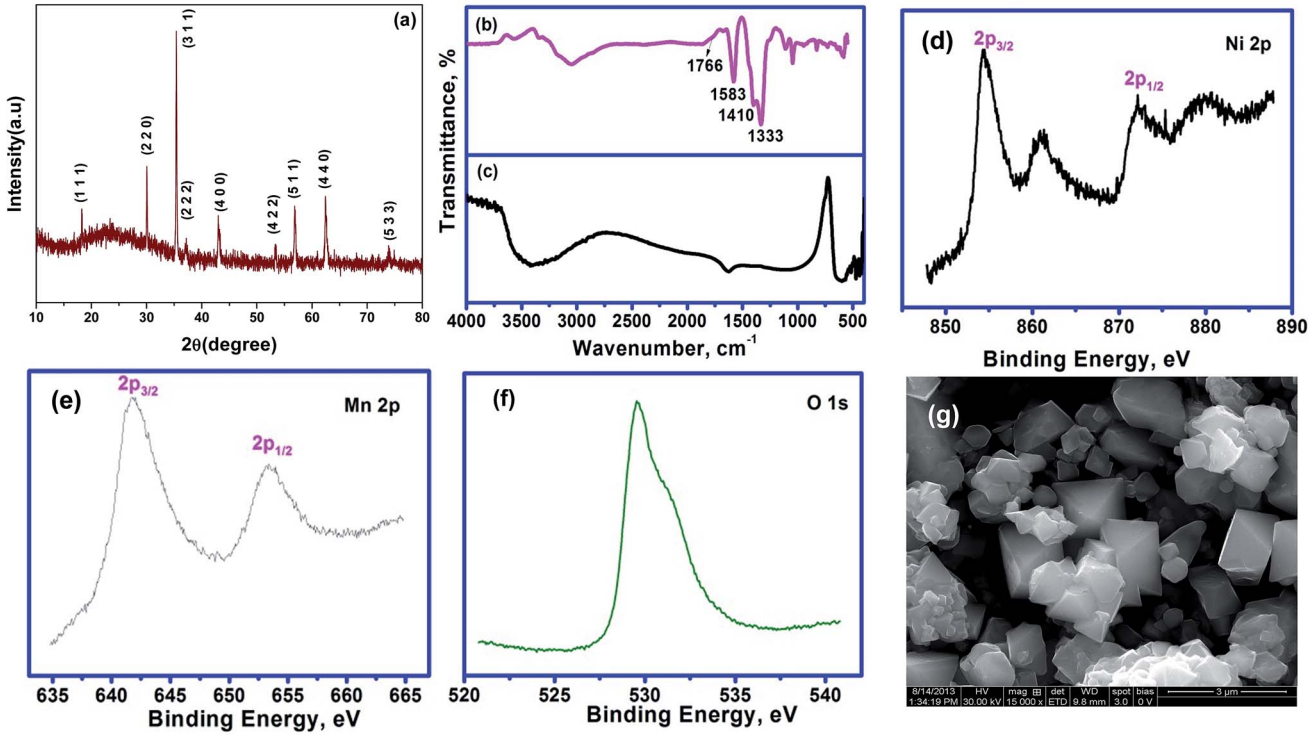

Fig. 1 X-ray diffraction (a), FT-IR spectra of before (b) and after (c) combustion, XPS spectra of the convoluted Ni (d), Mn (e), O (f) and FESEM image (f) of $NiMn_2O_4$.

$\sim$3500 cm^{-1} and $\sim$1600 cm^{-1} corresponds to O–H stretching and bending vibration of surface adsorbed water molecules, respectively. This surface adsorbed water molecules facilitate the wettability of the electrode which improved the electrochemical performances. Interestingly, no other organic functional groups were observed after combustion reaction, which confirms the complete burning of organic residues during combustion reaction.

The X-ray photoelectron spectroscopy is used to identify the surface composition of $NiMn_2O_4$ and the convoluted spectrum of Ni, Mn and O are given in (Fig. 1(d–f)). It can be seen that Ni shows two different binding energies at 854.47 eV for Ni $2p_{3/2}$ state and 872.05 eV corresponds to Ni $2p_{1/2}$ state. Similarly, the Mn also shows two binding energy peaks at 641.78 eV and 653.43 eV are ascribed to the Mn $2P_{3/2}$ and Mn $2P_{1/2}$, respectively. The O 1s peak is observed at 529.57 eV. Overall, the XPS spectra also confirms the formation of $NiMn_2O_4$ in pure phase.[26a,b]

Fig. 1(g) shows the FE-SEM images of $NiMn_2O_4$. It shows the formation of submicron size polyhedral shape individual particles with partial agglomeration. It can also be seen that the presence of octahedral shape particles, which may be formed by the assembly of primary particles.[26c] Normally, combustion synthesis provides agglomerated nanosized particles without any crystallographic shape. Interestingly, in the present work it is observed the formation of polyhedral shape $NiMn_2O_4$ particles.

Electrical properties

Fig. 2 shows the Cole–Cole plot of $NiMn_2O_4$ measured from room temperature to ambient temperature (180 °C). The observed single semicircle at the middle frequency region is due to the parallel combination of bulk resistance (R_b) and bulk capacitance (C_b) for all the temperature conditions. The R_b value is easily measured from the intersection of semicircle on the x-axis at low frequency or diameter of the semicircle. The intersection of the semicircle on the x-axis is shifted towards high frequency region while increasing the measuring temperature. This decrease in R_b with increasing temperature infers the semiconducting negative temperature co-efficient of resistance (NTCR) behaviour of $NiMn_2O_4$ crystals. It is well known that at room temperature, the grain boundary resistance is dominant for conduction. Subsequently, the grain boundary effect gets diminished with increasing temperature in turn causing high conductivity.[27,28] Hence, the grain size and nature of grain boundary plays a vital role for the electrical conductivity.[29–32] Using Cole–Cole plot, the d.c. conductivity is calculated and the maximum conductivity obtained was 1.1564×10^{-5} S cm^{-1} at 180 °C. The room temperature conductive behaviour of the material reveals that the $NiMn_2O_4$ will be a suitable material for energy storage applications.

Electrochemical properties of $NiMn_2O_4$ (3 electrode system)

In order to understand the electrochemical performance and charge storage kinetics of $NiMn_2O_4$ for energy storage applications, cyclic voltammetry (CV) was carried out at different scan rates and are shown in Fig. 3(a). The observed rectangular CV curve reveals that $NiMn_2O_4$ electrode is having good electrochemical reversibility and low internal resistance. Further, the rectangularity of the CV curve is maintained even at higher scan

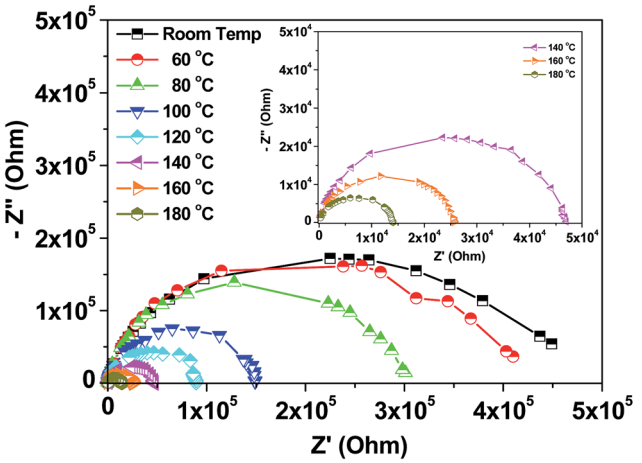

Fig. 2 Cole–Cole plot of $NiMn_2O_4$ at various temperatures (room temperature to 180 °C) and inset is the enlarged view.

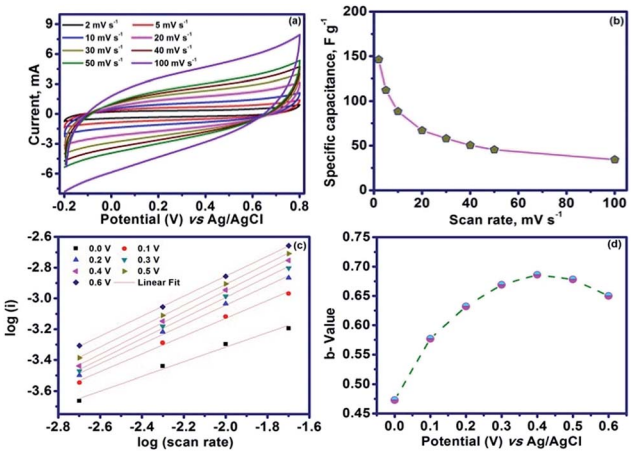

Fig. 3 Voltammetric response of $NiMn_2O_4$ (a) at different scan rate, (b) variation of specific capacitance as a function of scan rate, (c) variation of log(*i*) *vs.* log(scan rate) for Power's law, and (d) *b*-value plotted as a function of different potentials.

rate which reveals the good electrochemical performance of the electrode. In addition, there is no O_2 or H_2 gas evolution observed at the edges of switching potential. It reveals that the $NiMn_2O_4$ electrode can work in the wide range of potential window from −0.2 to 0.8 V without any damage. It is well known that area under the CV curve implies the total amount of charge stored based on pseudocapacitive and ion adsorption/desorption reaction. Subsequently, the CV curve justifies that the current rate increases with increasing scan rate. From CV curve, the obtained specific capacitance is 146 F g^{-1} at 2 mV s^{-1}. Fig. 3(b) shows the variation of specific capacitance with scan rate. It shows that at low scan rate, the electrode provides good and higher capacitance. But at higher scan rate, the electrode gives the lower specific capacitance. The reason for the variation of specific capacitance with scan rate is reported else where.[7] At low scan rate, the ions from electrolyte are having unlimited time to access the electrode both inside and outside surface, which leads to accommodating more number of ions into the electrode. Subsequently, at higher scan rates, the ions have ability to access only the outer surface of the electrode due to the limited time. Hence, the electrode exhibit lower specific capacitance at higher scan rates. Thus it reveals that the specific capacitance of the electrode material highly depends on the scan rate.

Generally, the CV current is the combination of both capacitive as well as intercalation/de-intercalation currents. Hence, the total amount of charge stored in the electrode is due to the combination of both capacitive and intercalation mechanisms. As well as, the capacitive mechanism consists of two different processes like surface redox or pseudocapacitive and ion adsorption/desorption at the electrode and electrolyte interface. According to Power's law, the scan rate dependence of CV current can be expressed as[33–35]

$$i = dv^b \quad (1)$$

where, v is scan rate (V s^{-1}), d and b are the adjustable parameters. The 'b' value can be determined from the slope of linear fit of log i *vs.* log v plot at a fixed potential (V). It is well known that the b value has two conditions, like $b = 0.5$ for intercalation/de-intercalation of ions into/from the electrode or diffusion controlled process and $b = 1$ for capacitive process or non-diffusive controlled process.[33–35] This is the best way to know the charge storage mechanism of electrode in each potential. Fig. 3(c) represents the plot between log i *vs.* log v at different potentials. It shows that the value of b is closer to 0.5 at each potential and is shown in Fig. 3(d). It evidenced that the intercalation of ions dominate for storing charge at all potentials rather than capacitive mechanism. Hence, the CV current is directly proportional to the square root of scan rate. The charge storage mechanism of $NiMn_2O_4$ is explained based on intercalation/de-intercalation mechanism as[17]

$$NiMn_2O_4 + Na^+ + e^- \leftrightarrow NaNiMn_2O_4 \quad (2)$$

It explains that during charging process the Na^+ ions from the electrolyte intercalate into $NiMn_2O_4$ matrix and release one electron. On the other hand, during discharging Na^+ ions are de-intercalated from $NiMn_2O_4$ matrix and diffuse into the electrolytic solution. It is well known that the scan rate dependent intercalation/de-intercalation and capacitive current can be explained using the following expression[33–35]

$$i\,(V) = k_1(v) + k_2(v^{1/2}) \quad (3)$$

where, $k_1(v)$ and $k_2(v^{1/2})$ represents the capacitive current and intercalation/de-intercalation current, which can be obtained by modifying the above equation.

$$i\,(V)/v^{1/2} = k_1(v^{1/2}) + k_2 \quad (4)$$

where, k_1 and k_2 corresponds to the slope and intercept of the linear fit of the plot between $i\,(V)/v^{1/2}$ and $v^{1/2}$. Once we know the values of k_1 and k_2, the current contribution through the intercalation/de-intercalation and capacitive mechanism can be easily distinguished at each potential. The shaded area of Fig. 4(a) implies the current contributed from capacitive

mechanism. Similarly, the un-shaded current area reveals the charge storage based intercalation/de-intercalation mechanism. Overall, it can be concluded that the maximum amount of charge is stored based on intercalation/de-intercalation mechanism rather than capacitive mechanism. This behaviour is well substantiated by the calculated "*b*" values from the CV curves.

Fig. 4(b) shows the total capacitance through intercalation and capacitive mechanism with scan rate. It reveals that the maximum amount of specific capacitance is derived from intercalation mechanisms rather than capacitive mechanism at low scan rate of 2 mV s^{-1}, *i.e.*, the electrode stores 91% of charge based on intercalation mechanism and 9% of charge based on capacitive mechanism. On the other hand, while increasing scan rate, the specific capacitance contribution from capacitive mechanism increased and decreased the capacitance contribution from intercalation mechanism. However, while increasing scan rate, the capacitive current increased gradually and intercalation current decreases and *vice versa*. It indicates that at high scan rate, the electrolyte ions do not have sufficient time to intercalate/de-intercalate into/from the $NiMn_2O_4$ matrix. Hence, the electrolyte ions undergo adsorption/desorption at the electrode/electrolyte interface. Overall, it is believed that the intercalation/de-intercalation mechanism is more dominant than capacitive mechanism at low scan rate and *vice versa*.

Further, the amount of specific capacitance contributed from inner and outer surface of the electrode is calculated using Trassati equation. According to Trassati, the total specific capacitance is the sum of specific capacitance provided by inner and outer surface of the electrode. It can be expressed as[6,36–39]

$$C_{\text{total}} = C_{\text{in}} + C_{\text{out}}\ (\text{F g}^{-1}) \quad (5)$$

The specific capacitance contributed from inner and outer surface of the electrode is dependent upon the scan rate (ν). The intercept ($\nu = 0$) of C_{total} *vs.* $\nu^{1/2}$ plot exhibits the total specific capacitance, since the diffusion of electrolyte ions into the electrode is uncontrolled (Fig. 4(c)). Similarly, the specific capacitance contributed by the outer surface is obtained from the intercept ($\nu = \infty$) of C_{out} *vs.* $\nu^{-1/2}$ plot because the diffusion of ions into the electrode is controlled (Fig. 4(d)). The calculated total and outer surface specific capacitance exhibited by the electrode is 137 and 22 F g^{-1} respectively. Hence, the specific capacitance exhibited by the inner surface of the electrode is 115 F g^{-1}. It reflects that more number of active sites is present in the inner surface of the electrode due to the intercalation of ions. This may be due to the presence of surface adsorbed water molecules which facilitate the increase in ionic diffusivity and accessibility into the electrode.

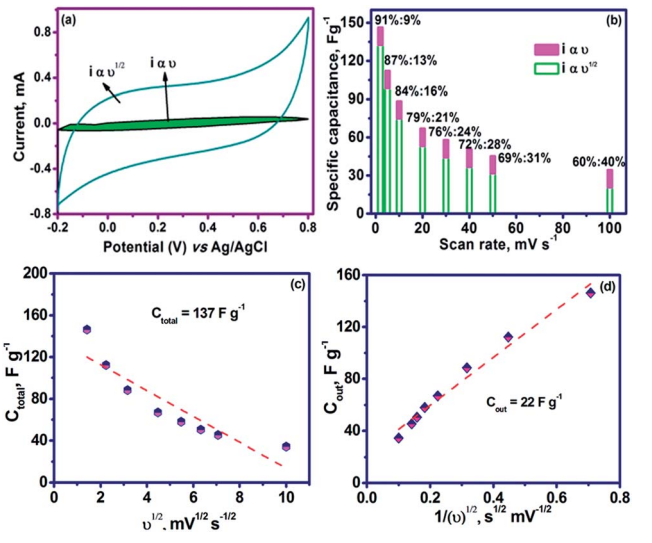

Fig. 4 (a) Comparative total current obtained experimentally (solid line) and capacitive current (shaded area), (b) variation of capacitive and intercalation specific capacitance as a function of scan rate, and (c and d) Trassati plot for calculation specific capacitance contribution of total and outer surface of the electrode.

In order to further support the CV results, the galvanostatic charge–discharge (GCD) analysis were carried out in 1 M Na_2SO_4 electrolyte. Fig. 5(a) shows the GCD curves of $NiMn_2O_4$ at different current densities such as 0.5, 0.7, 1, 2, 3, 4, and 5 mA cm^{-2}. The partial symmetric behaviour of the GCD curve resembles good reversibility of $NiMn_2O_4$. There is no significant IR drop observed at the beginning of discharge time even at high current density. It evidenced that the electrode material is having low internal resistance and energy loss. The maximum obtained specific capacitance is 202 F g^{-1} at a current density of 0.5 mA cm^{-2}. The obtained specific capacitance is higher than the reported values of 180 F g^{-1} at 250 mA g^{-1}, 94 F g^{-1} at 1 mV s^{-1}.[17,18] At low current density, (Fig. 5(b)) the obtained maximum specific capacitance is due to the ions from electrolyte which access both inner and outer surface of the electrode material. On the other hand, the specific capacitance is low at higher current densities due to inaccessibility of ions into inner surface of the electrode material. The obtained maximum energy density is 28.055 W h kg^{-1} at a power density of 250 W kg^{-1}. In order to further substantiate the GCD results, the area occupied by hydrated Na^+ ions on the surface of the electrode material is calculated[36] and are given in Fig. 5(c). It indicates that at low current density, a large area is occupied by the Na^+ hydrated ions on the surface. It is because the ions from electrolyte have enough time to interact with the active electrode which in turn causes a high specific capacitance. Similarly, the increase in current density leads to a decrease in the area occupied by ions on the surface of the electrode material. It is due to the limited accessibility of ions into the electrode which leads to the decrease in specific capacitance at higher current density.

The cyclic stability of the $NiMn_2O_4$ electrode is studied up to 15 000 cycles (Fig. 6) in 1 M Na_2SO_4 electrolyte at a current density of 5 mA cm^{-2}. During initial cycles, the specific capacitance of the electrode is found to increased with increasing cycles. This is the normal behaviour of the oxide materials, which may be due to the phase transition or morphological changes or activation effect in the electrode material.[7,40,41] Subsequently, the specific capacitance of the electrode is uniformly maintained upto 15 000 cycles. Similarly, the electrode provides the 100% Coulombic efficiency. The obtained cycling stability is comparatively excellent when compared with the previous reports.[42–49] Especially, Zhao *et al.* has reported that

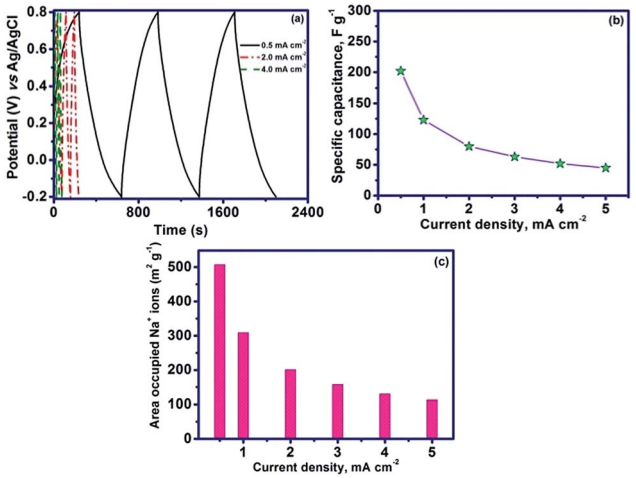

Fig. 5 (a) Galvanostatic charge–discharge curves at different current densities, (b and c) variation of specific capacitance and area occupied hydrated Na^+ ions on/in the surface of the electrode with current densities.

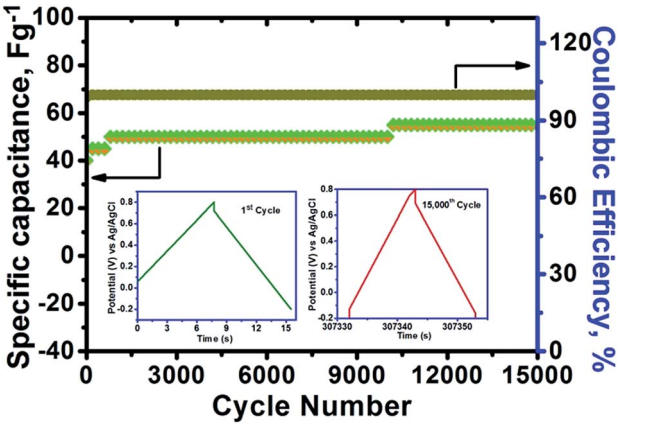

Fig. 6 Cyclic stability of $NiMn_2O_4$ over 15 000 cycles at 5 mA cm^{-2} in 1 M Na_2SO_4 electrolyte and inset corresponds to 1st and 15 000th cycle GCDs curve.

the N-doped graphene/Fe_2O_3 composite exhibited the cycle life of 82.5% over 1000 cycles.[42] Ray *et al.* prepared the titania nanotube/CoS composite using electrodeposition method which delivered 80% capacitance retention over 1000 cycles.[43] Using successive ionic layer adsorption and reaction method, α-La_2O_3 was prepared that provided 85% of initial specific capacitance over 1000 cycles.[44] The carbon@MnO_2 core–shell structured electrode showed 74% of capacitance retention after 2000 cycles.[45] The Sb-doped SnO_2 coated MnO_2 exhibited 88.4% of initial specific capacitance after 1000 cycles.[46] The N-doped graphene hollow sphere delivered 96% of initial specific capacitance even after 5000 cycles.[47] $Ni(OH)_2$/graphene/Ni foam electrode showed only 51% of specific capacitance retention after 500 cycles.[48] Min *et al.* has prepared $Ni(OH)_2$–RGO, which showed 90.6% of cycling stability over 5000 cycles.[49] Zhu *et al.* has prepared reduced graphene oxide/β-MnO_2 using hydrothermal method and reported 96.3% of initial specific capacitance after 10 000 cycles.[50] The NiO/Co_3O_4 showed 90% over 3000 cycles.[51] In the present case, the obtained high energy density and cycle life may be due to the polyhedral morphology, high electronic conductivity and method of synthesis. Overall, the good electrochemical performance and excellent cyclic stability embosses that the prepared $NiMn_2O_4$ electrode material is suitable for supercapacitors applications.

Electrochemical performances of fabricated asymmetric supercapacitor

In order to further exploit the scope of the prepared $NiMn_2O_4$ electrode, an asymmetric supercapacitor is fabricated and studied its detailed electrochemical performances and cycling stability. In this regard, $FeVO_4$ is used as the negative electrode for the fabrication. It is well known that the Fe based compounds will work in the negative window due to the redox reaction of Fe^{2+}/Fe^{3+} species. The synthesis, structural, electrical and electrochemical properties of the prepared $FeVO_4$ is given elsewhere.[52,53] Fig. 7(a) shows the CV curve of the fabricated device at different working potential windows of 1, 1.2, 1.4 and 1.5 V at 5 mV s^{-1}. It can be seen that no H_2/O_2 evolution is observed in the reduction/oxidation reactions, which indicates the optimal potential window of the device is 1.5 V. The CV curves of device at different scan rates are shown in Fig. 7(b). The CV current is increased with increasing scan rate indicates that the direct proportionality between CV current and scan rates. The calculated specific capacitance is 50 F g^{-1} at 1 mV s^{-1}. Subsequently, the specific capacitance of the device is decreased with increasing scan rate (Fig. 7(c)). It is the normal behaviour which occurred due to the less interaction time between the electrode and electrolyte ions.

Subsequently, the GCD analysis is carried out at different current densities of 0.5, 1 and 3 mA and is given in Fig. S1(a).† It is observed that the discharge time is decreased while increasing current densities. The calculated specific capacitances are 50, 40, 35, 32, 24, 16, and 13 F g^{-1} at 0.2, 0.3, 0.4, 0.5, 1, 2, and 3 mA, respectively. Further, the energy (E_{cell}) and power

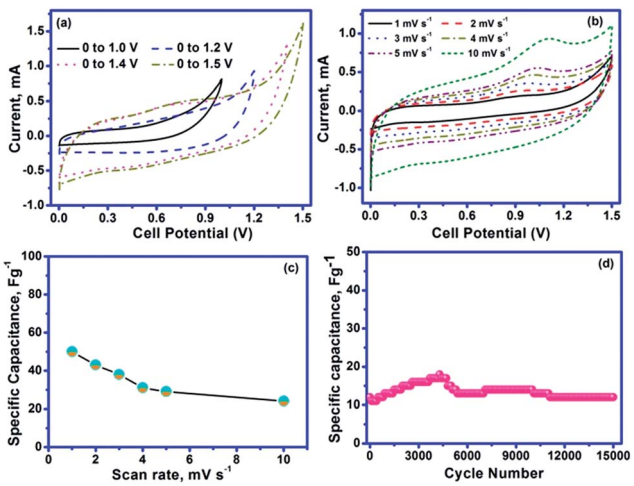

Fig. 7 (a and b) CV curves of asymmetric device at different working potential and various scan rates, (c) variation of specific capacitance with scan rates, (d) cycle life of the device over 15 000 cycles.

(P_{cell}) density is calculated.[54] The calculated maximum energy and power density is 15.625 W h kg^{-1} and 1125 W kg^{-1}, respectively (Fig. S1(b)†). The cyclic stability of the device is (Fig. 7(d)) investigated over 15 000 cycles at 3 mA. During initial cycling, the specific capacitance of the device is increased due to the activation effect or increasing wettability and started to decrease further cycling.[55] However, above 10 000 cycles, it maintains the initial capacitance. The obtained cycling stability is comparatively better than the existing literatures.[56–62] Overall, the fabricated asymmetric $FeVO_4$||$NiMn_2O_4$ supercapacitor is the best combination which can work upto 1.5 V in aqueous electrolyte. This enhanced potential window of the device may be due to the best combination of positive ($NiMn_2O_4$) and negative ($FeVO_4$) electrode.

4. Conclusion

Polyhedral shape $NiMn_2O_4$ particles were successfully prepared using glycine assisted combustion method. The XRD and FT-IR confirms the formation of single phase of $NiMn_2O_4$. The Cole–Cole plot revealed that $NiMn_2O_4$ is having a semiconductor nature as well as NTCR behaviour as its conductivity increases with increase in temperature. Subsequently, the intercalation/de-intercalation mechanism was identified as a dominant mechanism for storing charge in $NiMn_2O_4$ rather than capacitive mechanism. The obtained higher specific capacitance (202 F g^{-1}), energy density (28.055 W h kg^{-1}), and good cyclic stability elaborates that $NiMn_2O_4$ is suitable electrode material for supercapacitor applications. Subsequently, the fabricated device exhibits good specific capacitance (50 F g^{-1} at 1 mV s^{-1}) and energy density (15 W h kg^{-1}). The device delivers excellent specific capacitance retention over 15 000 cycles.

Acknowledgements

The authors would like to thank Department of Science and Technology (DST-SERB), Government of India, for providing Financial support (SR/FTP/PS-80/2009) under the "Fast Track Young Scientist" scheme.

Notes and references

1 V. Augustyn, P. Simon and B. Dunn, *Energy Environ. Sci.*, 2014, **7**, 1597–1614.
2 G. Wang, L. Zhang and J. Zhang, *Chem. Soc. Rev.*, 2012, **41**, 797–828.
3 K. Naoi, S. Ishimoto, J. Miyamoto and W. Naoi, *Energy Environ. Sci.*, 2012, **5**, 9363–9373.
4 M. Zhi, C. Xiang, J. Li, M. Li and N. Wu, *Nanoscale*, 2013, **5**, 72–88.
5 F. Béguin and E. Frqckowiak, *Supercapacitors Materials, Systems, and Applications*, Wiley-VCH Verlag GmbH & Co. KGaA, Boschstr, Weinheim, Germany, 2013, vol. 12, p. 69469.
6 M. Rajesh, K. V. Sankar, S. M. Chen and R. K. Selvan, *RSC Adv.*, 2014, **4**, 1225–1233.
7 K. V. Sankar, D. Kalpana and R. K. Selvan, *J. Appl. Electrochem.*, 2012, **42**, 463–470.
8 Y. Zhang, L. Li, H. Su, W. Huang and X. Dong, *J. Mater. Chem. A*, 2015, **3**, 43–59.
9 D. Liu, X. Wang, X. Wang, W. Tian, J. Liu, C. Zhi, D. He, Y. Bando and D. Golberg, *J. Mater. Chem. A*, 2013, **1**, 1952–1955.
10 V. S. Kumbhar, A. D. Jagadale, N. M. Shinde and C. D. Lokhande, *Appl. Surf. Sci.*, 2012, **259**, 39–43.
11 P. Sena and A. Deb, *Electrochim. Acta*, 2010, **55**, 4677–4684.
12 S. L. Kuo and N. L. Wu, *Electrochem. Solid-State Lett.*, 2007, **10**, A171–A175.
13 A. Shanmugavani and R. K. Selvan, *RSC Adv.*, 2014, **4**, 27022–27029.
14 S. K. Meher and G. Ranga Rao, *J. Phys. Chem. C*, 2011, **115**, 25543–25556.
15 Y. Lei, Y. Wang, W. Yang, H. Yuan and D. Xiao, *RSC Adv.*, 2015, **5**, 7575–7583.
16 Y. Xu, X. Wang, C. An, Y. Wang, L. Jiao and H. Yuan, *J. Mater. Chem. A*, 2014, **2**, 16480–16488.
17 H. Pang, J. Deng, S. Wang, S. Li, J. Du, J. Chen and J. Zhang, *RSC Adv.*, 2012, **2**, 5930–5934.
18 Y. Ren, Z. Ma and P. G. Bruce, *CrystEngComm*, 2011, **13**, 6955–6959.
19 M. Zhang, S. Guo, L. Zheng, G. Zhang, Z. Hao, L. Kang and Z. H. Liu, *Electrochim. Acta*, 2013, **87**, 546–553.
20 Menaka, N. Garg, S. Kumar, D. Kumar, K. V. Ramanujachary and S. E. Lofland, *J. Mater. Chem.*, 2012, **22**, 18447–18453.
21 M. Zhang, S. Guo, L. Zheng, G. Zhang and Z. Hao, *Electrochim. Acta*, 2013, **87**, 546–553.
22 A. Diez, R. Schmidt, A. E. Sagua, M. A. Frechero, E. Matesanz, C. Leon and E. Moran, *J. Eur. Ceram. Soc.*, 2010, **30**, 2617–2624.
23 P. K. Sharma, R. K. Dutta, R. J. Choudhary and A. C. Panday, *CrystEngComm*, 2013, **15**, 4438–4447.
24 V. S. Kumbhar, A. D. Jagadale, N. M. Shinde and C. D. Lokhande, *Appl. Surf. Sci.*, 2012, **259**, 39–43.
25 A. Baykal, H. Deligoz and H. Sozeri, *J. Supercond.*, 2012, **25**, 1879–1892.
26 (*a*) Y. Guan, C. Yin, X. Cheng, X. Liang, Q. Diao, H. Zhang and G. Lu, *Sens. Actuators, B*, 2014, **193**, 501–508; (*b*) M. Zhang, S. Guo, L. Zheng, G. Zhang, Z. Hao, L. Kang and Z. H. Liu, *Electrochim. Acta*, 2013, **87**, 546–553; (*c*) H. Jiang, T. Zhao, C. Yan, J. Ma and C. Li, *Nanoscale*, 2010, **2**, 2195–2198.
27 C. Bose, P. Balaya, P. Thangadurai and S. Ramasamy, *J. Phys. Chem. Solids*, 2003, **64**, 659–663.
28 M. Manikandan and C. Venkateswaran, *J. Magn. Magn. Mater.*, 2014, **358–359**, 82–86.
29 R. O. Fuentes, F. M. Figueiredo, F. M. B. Marques and J. I. Franco, *Solid State Ionics*, 2001, **140**, 173–179.
30 S. Brahma, R. N. P. Choudhary and A. K. Thakur, *Phys. B*, 2005, **355**, 188–201.
31 S. Sen and R. N. P. Choudhary, *Mater. Chem. Phys.*, 2004, **87**, 256–263.
32 P. S. Anantha and K. Hari Haran, *Mater. Chem. Phys.*, 2005, **89**, 428–437.

33 M. Sathiya, A. S. Prakash, K. Ramesh, J. M. Tarascon and A. K. Shukla, *J. Am. Chem. Soc.*, 2011, **133**, 1629–16299.
34 J. Duay, S. A. Sherrill, Z. Gui, E. Gillette and S. B. Lee, *ACS Nano*, 2013, **7**, 1200–1214.
35 H. Yina, C. Song, Y. Wang, S. Li, M. Zeng, Z. Zhang, Z. Zhu and K. Yu, *Electrochim. Acta*, 2013, **111**, 762–770.
36 K. V. Sankar and R. K. Selvan, *RSC Adv.*, 2014, **4**, 17555–17566.
37 K. V. Sankar and R. K. Selvan, *J. Power Sources*, 2015, **275**, 399–407.
38 B. Senthilkumar, K. V. Sankar, C. Sanjeeviraja and R. K. Selvan, *J. Alloys Compd.*, 2013, **553**, 350–357.
39 B. Senthilkumar, K. V. Sankar, L. Vasylechko, Y. S. Lee and R. K. Selvan, *RSC Adv.*, 2014, **4**, 53192–53200.
40 K. V. Sankar, S. T. Senthilkumar, L. J. Berchmans, C. Sanjeeviraja and R. K. Selvan, *Appl. Surf. Sci.*, 2012, **259**, 624–630.
41 D. P. Dubal, D. S. Dhawale, R. R. Salunkhe, S. M. Pawar and C. D. Lokhande, *Appl. Surf. Sci.*, 2010, **256**, 4411–4416.
42 P. Zhao, W. Li, G. Wang, B. Yu, X. Li, J. Bai and Z. Ren, *J. Alloys Compd.*, 2014, **604**, 87–93.
43 R. S. Ray, B. Sarma, A. L. Jurovitzki and M. Misra, *Chem. Eng. J.*, 2015, **260**, 671–683.
44 S. J. Patil, V. S. Kumbhar, B. H. Patil, R. N. Bulakhe and C. D. Lokhande, *J. Alloys Compd.*, 2014, **611**, 191–196.
45 Y. Zhao, Y. Meng and P. Jiang, *J. Power Sources*, 2014, **259**, 219–226.
46 Y. Zhang and Y. Mo, *Electrochim. Acta*, 2014, **142**, 76–83.
47 W. Fan, Y. Y. Xia, W. W. Tjiu, P. U. Pallathadka, C. He and T. Liu, *J. Power Sources*, 2013, **243**, 973–981.
48 L. Wang, X. Li, T. Guo, X. Yan and B. K. Tay, *Int. J. Hydrogen Energy*, 2014, **39**, 7876–7884.
49 S. Min, C. Zhao, Z. Zhang, G. Chen, X. Qian and Z. Guo, *J. Mater. Chem. A*, 2015, **3**, 3641–3650.
50 S. Zhu, H. Zhang, P. Chen, L. H. Nie, C. H. Li and S. K. Li, *J. Mater. Chem. A*, 2015, **3**, 1540–1548.
51 K. Wang, Z. Zhang, X. Shi, H. Wang, Y. Lu and X. Ma, *RSC Adv.*, 2015, **5**, 1943–1948.
52 V. D. Nithya, R. Kalai Selvan, C. Sanjeeviraja, D. Mohan Radheep and S. Arumugam, *Mater. Res. Bull.*, 2011, **46**, 1654–1658.
53 V. D. Nithya and R. Kalai Selvan, *Phys. B*, 2011, **406**, 24–29.
54 B. Senthilkumar, D. Meyrick, Y. S. Lee and R. K. Selvan, *RSC Adv.*, 2013, **3**, 16542–16548.
55 Y. J. Peng, T. H. Wu, C. T. Hsu, S. M. Li, M. G. Chen and C. C. Hu, *J. Power Sources*, 2014, **272**, 970–978.
56 J. Ji, L. L. Zhang, H. Ji, Y. Li, X. Zhao, X. Bai, X. Fan, F. Zhang and R. S. Ruoff, *ACS Nano*, 2013, **7**, 6237–6243.
57 H. Gao, F. Xiao, C. B. Ching and H. Duan, *ACS Appl. Mater. Interfaces*, 2012, **4**, 2801–2810.
58 J. Shen, C. Yang, X. Li and G. Wang, *ACS Appl. Mater. Interfaces*, 2013, **5**, 8467–8476.
59 M. Kim and J. Kim, *Phys. Chem. Chem. Phys.*, 2014, **16**, 11323–11336.
60 C. Yang, M. Zhou and Q. Xu, *Phys. Chem. Chem. Phys.*, 2013, **15**, 19730–19740.
61 C. Dong, Y. Wang, J. Xu, G. Cheng, W. Yang, T. Kou, Z. Zhang and Y. Ding, *J. Mater. Chem. A*, 2014, **2**, 18229–18235.
62 H. Wang, H. Yi, X. Chen and X. Wang, *J. Mater. Chem. A*, 2014, **2**, 3223–3230.